

# Rapid Bending Origami in Micro/Nanoscale toward a Versatile 3D Metasurface

Ruhao Pan, Zhancheng Li, Zhe Liu, Wei Zhu, Liang Zhu, Yunlong Li, Shuqi Chen, Changzhi Gu,\* and Junjie Li\*

Devices consisting of 3D components are always desired for their far more controllable degrees of freedom compared with their planar counterparts; however, the limitations on the fabrication of 3D nanostructures have severely restricted their applications. Here, a focused ion beam (FIB) defined rapid bending origami method is reported to fabricate 3D micro/nanoscale architectures, by relying on ion irradiation induced 2D structure bending mechanism based on the residual stress formation in metal/dielectric film. Regulated by ions irradiation dose and energy, a large-scale programmable 2D patterns can be controllably bended to configure versatile 3D micro/nanostructures with scalable bending capacity and feature sizes down to 175 nm. The benefit of this method is, a 3D bended metasurface is designed and fabricated as an asymmetric mirror, showing a very simple strategy to realize high-efficiency unidirectional reflectionless effect. This FIB-defined bending origami proves to be a rapid fabrication approach of varied 3D configuration in micro/nanoscale with extremely flexible controllability of spatial orientation, providing more opportunities and options for various functional devices based on 3D configurations, especially for 3D metasurfaces.

mechanics, photonics, biology,<sup>[1–5]</sup> etc., which have been applied in the field of micro/nano-electromechanical,<sup>[6–9]</sup> biomedical devices,<sup>[10–13]</sup> and energy storage.<sup>[14]</sup> Notably, one of the most meaningful applications of 3D structures is in the field of 3D optical metamaterials,<sup>[5,15–17]</sup> having far more degrees of freedom in spatial modulation of electromagnetic wave compared to their 2D counterparts. The assembling of the 3D structures is mostly based on traditional fabrication processes with multilayer stacking of 2D pattern, for example, etching and deposition process based on lithography such as electron beam lithography (EBL) or ultraviolet lithography.<sup>[18–21]</sup> However, with the development of 3D metamaterials, the planar techniques are not enough to fabricate delicate 3D unit cells with flexible features such as suspended, free spatial orientation and reconfigurable properties. Fortunately, 3D structures can also

## 1. Introduction

In recent decades, 3D micro/nanostructures have attracted increasing and broad interests for their unique properties in

Dr. R. Pan, Dr. Z. Liu, W. Zhu, L. Zhu, Dr. Y. Li, Prof. C. Gu, Prof. J. Li  
Beijing National Laboratory for Condensed Matter Physics, Institute of Physics

Chinese Academy of Sciences

Beijing 100190, China

E-mail: czgu@iphy.ac.cn; jjli@iphy.ac.cn

Dr. R. Pan, L. Zhu, Prof. C. Gu, Prof. J. Li

School of Physical Sciences, CAS Key Laboratory of Vacuum Physics

University of Chinese Academy of Sciences

Beijing 100049, China

Dr. Z. Li, Prof. S. Chen

Laboratory of Weak Light Nonlinear Photonics

of the Ministry of Education, School of Physics and Teda Applied Physics Institute


Nankai University

Tianjin 300071, China

Prof. J. Li

Songshan Lake Materials Laboratory

Dongguan 523808, China

 The ORCID identification number(s) for the author(s) of this article can be found under <https://doi.org/10.1002/lpor.201900179>

DOI: 10.1002/lpor.201900179

take shape by a series of direct writing technologies including 3D printing and femtosecond laser writing, but these methods are under some restrictions of alternative materials, structure size, and machining efficiency, that is, the structures are usually constructed by polymer and the fabrication capacity is relatively low compared to the planar technologies; moreover, the feature size is hard to be realized in sub-micrometer for 3D printing method. All these limitations impede the invention of higher-performance 3D devices, especially for the components consisting of 3D structures with size down to several micrometers or even hundreds of nanometers. Besides, a mass-production process with low cost is also desired.

3D origami is a famous art technique based on bending or folding planar membranes or films into 3D complex and complicated configurations in macroscale.<sup>[22,23]</sup> Inspired by this idea to configure 3D origami in mesoscopic scale, a series of technologies have been developed, such as compressive buckling,<sup>[24–26]</sup> stress-mismatch induced bending,<sup>[27–29]</sup> and even capillary force and cell traction force induced bending.<sup>[30–33]</sup> By these technologies, delicate 3D structures can be constructed from 2D patterns by different driving forces. We know that the application of these 3D structures in modulators, sensors, or metamaterials has been widely studied,<sup>[34,35]</sup> but when these 3D structures to those devices are operating in mid/near-infrared and even visible region,

they need to have a sub-5  $\mu\text{m}$  feature size and even down to hundred nanometers with relatively large area. However, most of the above 3D folding technologies have difficulties in sub-5  $\mu\text{m}$  fabrication and not to mention hundred nanometers. Although these methods have achieved in complex 3D metamaterial fabrication based on the control of driving force and planar pattern design, the bending curvature is mainly determined by the thickness of the film and the stress of the materials,<sup>[27,36]</sup> and further the curvature radius is usually too large to get the sub-5  $\mu\text{m}$  structures. In order to obtain 3D origami structures with a smaller feature size, ion-induced self-organized origami is developed, and especially focused ion beam (FIB) technology is used to induce folding 2D structure into 3D architecture.<sup>[37,38]</sup> Noteworthy, based on our previous reports,<sup>[39]</sup> FIB induced folding possesses some obvious advantages in the beam spot resolution, fabricating precision, controllable ion energy, materials universality, and cross-scale fabrication, which is very useful for folding suspended 2D pattern into micro-nanoscale 3D structure and apply in near-infrared (NIR) and visible metamaterials.<sup>[40,41]</sup> However, due to a FIB local-irradiation mode and the FIB cutting process, slow fabricating speed in the FIB induced folding process is a big problem, and fabricating a 3D configuration array with comparable area usually takes hours or even longer, and thus a substantial improvement in FIB induced assembling 3D structure are urgently needed to fabricate rapidly scalable 3D micro/nanodevices.

In this work, we propose a FIB-induced bending technology in parallel with FIB-induced folding, developing into a FIB defined rapid origami method for the fabrication of 3D micro/nanostructures. This bending mode, based on FIB area-irradiation, shows much more superiority in rapid preparation, mass production, and good spatial controllability over folding mode controlled by FIB local-irradiation, and thus makes up the technical shortening of folding mode. And meanwhile, the combination of bending and folding can highlight a powerful capability in 3D fabrication. FIB-defined rapid bending origami mainly contains two processes: the planar process of 2D patterned freestanding membrane and FIB area-irradiation 2D pattern induced its bending toward the ion beam direction, and hence configuring a programmable 3D structure. Ions implantation by FIB in the bending region will cause the different stress distributions from the surface layer to deep layer of suspended membrane, and tensile stress in surface layer mainly determines the suspended 2D structure to bend upward with an accurately controllable curvature by ion irradiation. This FIB-defined origami method meets greatly the desire of configuring versatile 3D structures with a wide range of the size down to sub-1  $\mu\text{m}$ , which is especially suitable for design and fabrication of desirable 3D metasurface that is expected to realize unusual light field regulation for the applications in micro/nanophotonic device. Here, a kind of bended metasurface consisted of a bended nanocantilever and U-shaped hollow nanostructure is designed and configured as an asymmetric mirror, and a strong unidirectional reflectionless effect with high efficiency and tunable near-infrared absorption peak are achieved in the bended cantilevers structure arrays, showing a great application potential in biomedical, free-space optical communications, and remote sensing devices.

## 2. Results and Discussion

### 2.1. FIB-Defined Origami for 3D Micro/Nanostructure

The fabrication process of FIB rapid origami is depicted in **Figure 1a**, containing four steps from 2D film to 3D structure. The prepatterned Au/SiN<sub>x</sub> membrane is area irradiated by FIB and bended upward to configure 3D structure. As a consequence, a typical bending 3D structure with much larger curvature is obtained after FIB irradiation process, as shown from a colored scanning electron microscope (SEM) image in **Figure 1a**. In the above process, 2D patterns can be freely designed by advanced planar techniques, and various imaginative 3D micro/nanostructures can be assembled from 2D structure by FIB induced bending origami. **Figure 1b** shows SEM images of a crossed arm structure with a remarkable change in the curvature under increased ions doses. The feature size of this typical structure includes the thickness of the bilayer (Au/SiN<sub>x</sub>: 60/20 nm) and length-width ratio (2.5  $\mu\text{m}$ /300 nm) in single-arm. It can be seen that with increasing ion dose to  $6 \times 10^{14}$  ions  $\text{cm}^{-2}$ , the curvature of a crossed arm structure is significantly changed up to  $1.05 \mu\text{m}^{-1}$ . It is worth noting that, before FIB irradiation, Au deposition on the SiN<sub>x</sub> cantilever leads to a downward bending with small negative curvature, as shown in the first image of **Figure 1b**, which is attributed to a mismatch stress between SiN<sub>x</sub> layer and Au membrane. This mismatch stress induced bending has been reported,<sup>[36,42]</sup> and obtained by etching sacrificial layer under the Au/SiN<sub>x</sub> bilayer. However, the mismatch stress is too small to fabricate 3D structures with radius of curvature down to 1  $\mu\text{m}$ . Greater stress should be introduced into the bilayer system in order to enlarge the curvature. Among stress modulated methods, ion irradiation is an effective approach for controlling the stress in a micro-region.<sup>[39,43]</sup> To get a large stress on the bilayer system, ion beam irradiation is further introduced in the process. The quantitative relation between the bending curvature and other parameters such as the film thickness, ions energy, and ions dose, are presented in **Figure 1c,d**. **Figure 1c** depicts the bending curvature as a function of ions dose with different ion energies, finding that the curvature (or bending angle) is almost linearly proportional to the ion doses and ion energy. This is because ion beam with larger dose and higher energy would produce larger intruded-stress in the bilayer film. In addition, the curvature is also related to the thickness of the materials, as shown in **Figure 1d**. The thicker Au/SiN<sub>x</sub> bilayer is more disadvantageous to the bending deformation. However, in the case of the same film thickness, the curvature of a single layer of Au is a little more than that of Au/SiN<sub>x</sub> bilayer, and the thicker SiN<sub>x</sub> layer is not conducive to bending deformation for Au/SiN<sub>x</sub> bilayer. Besides, in order to ensure the consistency of the experiment, a Au single layer is obtained from the SiN<sub>x</sub> etching process of the Au/SiN<sub>x</sub> bilayer. It is found that the Au/SiN<sub>x</sub> film is already bended by the mismatch stress during the Au deposition, and thus a negative curvature can be observed for single layer Au.

Compared to a Au single layer for origami structures, the Au/SiN<sub>x</sub> bilayer shows several advantages as follows: 1) SiN<sub>x</sub> is a kind of dielectric with excellent mechanical properties, and the Au/SiN<sub>x</sub> bilayer structures are more robust than the Au single layer structures. 2) High quality freestanding SiN<sub>x</sub> film is easily obtained from wetting-etching or commercial way; however,

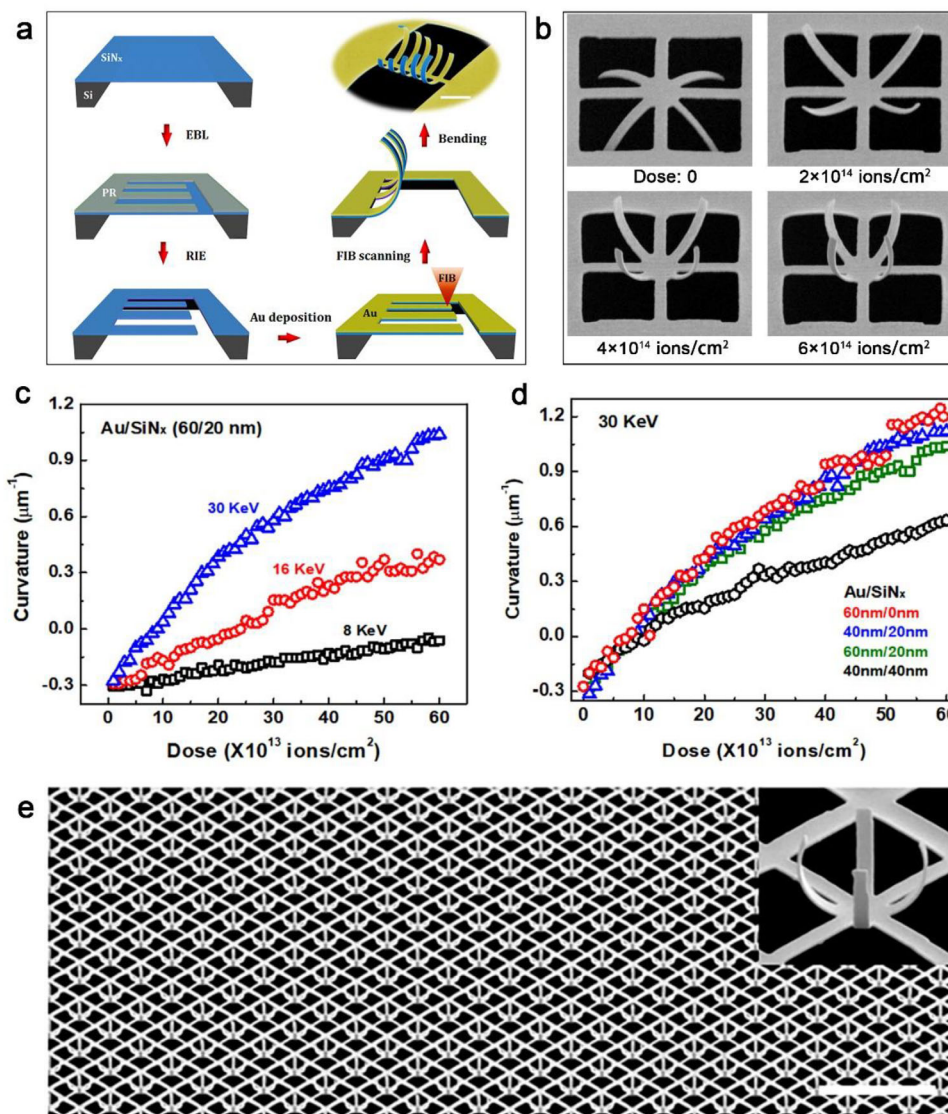


**Figure 1.** Fabrication and controllability of FIB-defined bending origami. a) Schematic of the technical process to fabricate 3D bending structure, including EBL, RIE, Au deposition, FIB irradiation, and bending deformation, a dotted line marked in FIB irradiation process indicating area-scanning; b) SEM images of a bending crossed arm structure with different curvatures under an increased ion irradiation dose; c) Curvature of the cantilever as a function with ion dose and energy and d) with different thicknesses and ions dose; e) SEM image of  $100.0 \times 100.0 \mu\text{m}^2$  sample of cross bending structure with good uniformity. Scale bar in (a) and (b):  $2 \mu\text{m}$ , (e)  $10 \mu\text{m}$ .

smooth self-supported gold film can hardly be obtained from a comfortable way. And thus Au is coated to the prepatterned  $\text{SiN}_x$  film as a bilayer film, which provides a convenient and reliable way to fabricate origami structures. 3)  $\text{SiN}_x$  layer has a good transparency and no obvious effect on the application in metasurface. Figure 1e displays a large-scale cross bending structure array with  $100.0 \times 100.0 \mu\text{m}^2$  size and good uniformity, which can be quickly completed in 30 s to fully demonstrate rapid fabrication capacity of this FIB-defined bending origami. Overall, it can be found that FIB-induced bending process is markedly different from previous FIB-induced folding process. FIB-induced folding relies on a local deformation realized by one-by-one FIB line-scanning, while FIB-induced bending depends on the global deformation realized by area-scanning. Thus, bending origami is

not only a quicker fabrication with a lower ions irradiation dose but also can support more spatial configurations compared with folding method, which is also the uniqueness of our proposed FIB-defined bending origami.

The main mechanism of FIB-defined bending origami is further analyzed, as schematically illustrated in Figure 2a. When the film is irradiated by FIB, a series of phenomenon would occur, such as surface sputtering and ion-implantation, together with local disordering or amorphization, vacancy defect and mass transport, etc.<sup>[44,45]</sup> as illustrated in the left of Figure 2a. Above ion-implantation induced effects will cause an uneven distribution of the stress, and as-generated residual stress in the film is a main mechanism of FIB-defined bending origami, as displayed in the right of Figure 2a. The distribution of the residual stress



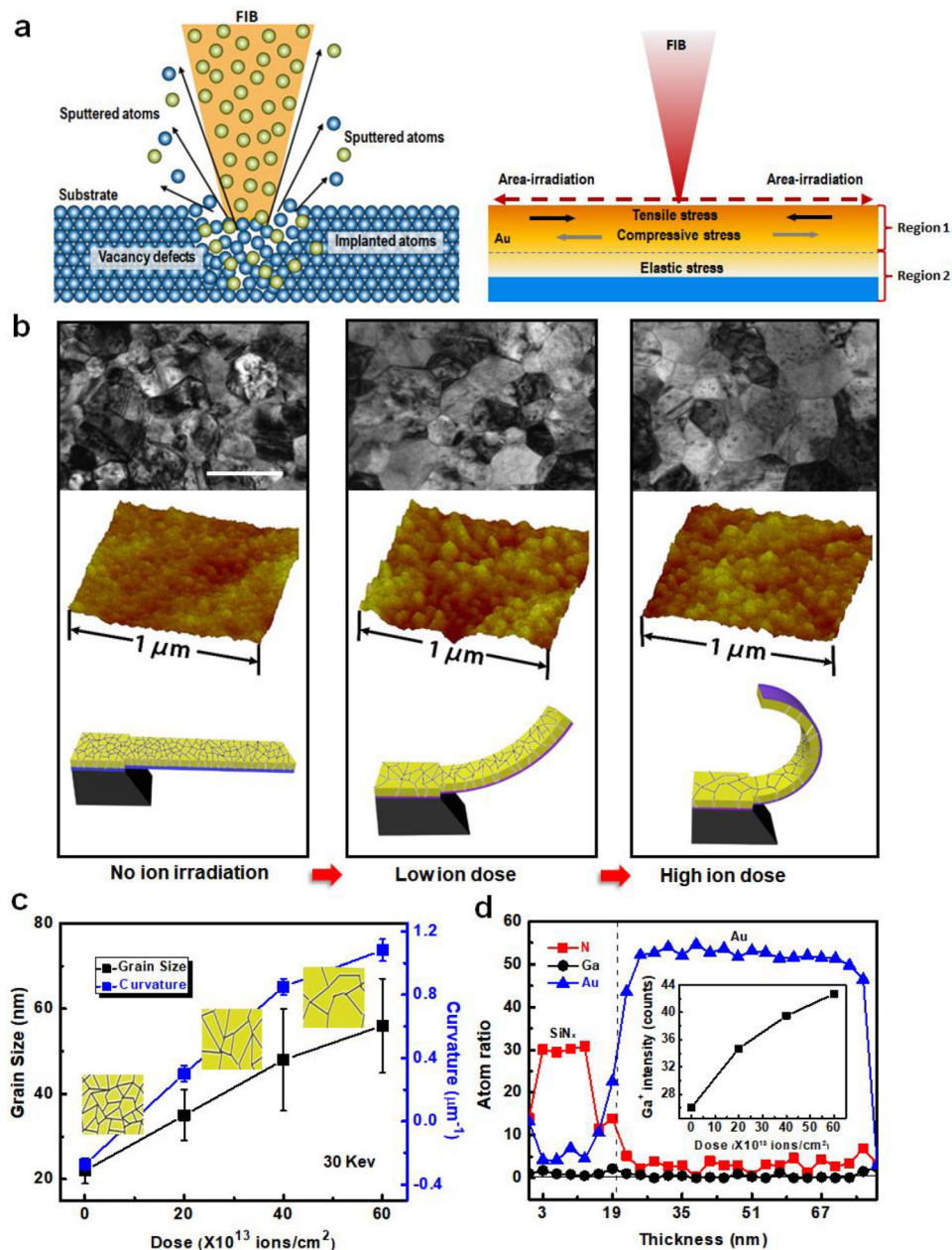


**Figure 2.** Analysis of the bending mechanism, morphology, and component of the FIB-defined origami process for Au/SiN<sub>x</sub> bilayer. a) Schematic illustration of FIB-matter interactions and residual stress distribution of Au/SiN<sub>x</sub> bilayer; b) Changes of the surface morphology of Au film with ions dose, including the grain sizes and surface topography characterized by TEM and AFM, respectively, as well as a schematic of the bending cantilever; c) Relationship between Au grain sizes together with curvatures and the ion dose; d) EDS analysis: Atom ratio of Au, N, and Ga distribution of a bending cantilever in the cross section, and an inset indicates the relative intensity of Ga peak ion changes with the ion irradiation dose. Scale bar in (b) 50 nm.

is divided into two regions from surface to deep layer of the film depending on the impact of ion-implantation. As-marked region-1 is much affected by FIB implantation, mass vacancy defects in the film surface produced by strong ion-bombardment sputtering together with ion-implantation will result in grain coalescence and then size variation, so that the large tensile stress can be dominantly induced in the surface layer of the film.<sup>[46]</sup> And meanwhile, ion-implantation causes atomic rearrangement in region-1 also creates additional compressive stress.<sup>[47]</sup> The

dominant tensile stress determines the bend upward compared with compressive stress. Corresponding to the plastic flow of region-1, region-2 shows the distribution of elastic stress because the one is affected quite little by FIB implantation, and as a consequence, the bending deformation is induced by contraction of the top layer.

Figure 2b gives a series of transmission electron microscopy (TEM) image of Au film surface with corresponding atomic force microscope (AFM) images and illustrated schematic of bending

deformation, showing clearly the evolution of surface topography and Au grains sizes with different ion doses for irradiation. The size of Au grains is increased evidently from  $\approx 20$  to  $\approx 60$  nm as ion dose is enhanced from 0 to  $6 \times 10^{14}$  ions  $\text{cm}^{-2}$ , along with the increased surface roughness and bending curvature, which is very consistent with the results predicted by above mechanism of ion-irradiation induced bending deformation. More importantly, this is a direct evidence of ion-implantation causing the coalescence and rearrangement of Au grains. Figure 2c summarizes the linear relationship between Au grain sizes together with curvatures and the ion dose, indicating that higher ions doses are bound to enhance the Au grain size and the bending curvature. Figure 2d gives an energy disperse spectroscopy (EDS) of a single cantilever bended by  $6 \times 10^{14}$  ions  $\text{cm}^{-2}$  irradiation, revealing the atomic ratio distribution of Au, N, and Ga in the bilayer film along the cross section. We can see that Ga is hardly detected in the EDS, indicating a very low Ga content compared with other elements in the ion-irradiated bilayer film. After a cumulative detection by increasing the sampling time, the signal intensity of Ga peak in the EDS can be plotted with the change of ions doses, as shown in the inset of Figure 2d, and a near-linear increase of Ga content with ions doses can be observed, which is broadly along our expectation.

Following this bending deformation mechanism above, in order to confirm the fabrication capacity of this method, a sequence of configurations is designed and fabricated by FIB-defined origami, as shown in Figure S1, Supporting Information. The results show that the bending architectures with different shapes yield to a same radius under the same ion irradiation, indicating the bending radius is independent to the shape of the cantilevers. Besides, bending structures with 175 nm radius can be fabricated by FIB defined bending, revealing the FIB defined bending method has the ability of fabricating nanoscale 3D structures. Particularly a multiple dimensions composite structures including folded cross-bending structure and cubical micro-cage arrays demonstrate fully the ability of flexibly powerful 3D fabrication of bending/folding origami. Thus the bending mode combined with folding mode will create more dimensional spatial structures, contributing to FIB-defined origami method for providing more chances and far-reaching effects on the design and manufacture of new-fashioned 3D devices. In addition, the mechanical stability of 3D bending structure is another issue of concern, and their related testing is carried out and as shown in Figure S2, Supporting Information, demonstrating a good stability in mechanical endurance.

## 2.2. Bended Metasurface Based on FIB-Defined Origami

The flexibility and controllability are the biggest advantages of FIB-defined bending origami method, providing a vast space for the application and development of various 3D functional devices, meeting greatly the desire of sub-1  $\mu\text{m}$  3D structure fabrication. Especially this method is very suitable for the configuration of versatile 3D metamaterials with free spatial orientations and optional chirality, which can be easily assembled by bending or folding from 2D pattern in micro/nanometer scale. Here, by FIB-defined bending origami method, we design and fabricate a new-type freestanding asymmetric mirror con-

sisting of 3D bended metasurface, realizing a high-efficiency asymmetric reflection property through a simple mechanism. Traditionally, the asymmetric reflection structures are composed of multilayer structures with materials of different indices or parity-time symmetric (PT) optical systems.<sup>[48–50]</sup> However, asymmetric mirrors assembled by multilayer materials are usually limited by the low efficiency in reflectance and difficult to achieve unidirectional reflectionless effect, while the spectral measurement of PT metamaterials need a horizontal incident light rather than normal vertical incidence, which is highly restricted experimentally.<sup>[51,52]</sup> The FIB-defined bending origami fabrication method proposes a shortcut to overcome the limitations of planar process in flexible and novel 3D micro-/nanostructures, and makes a suspended unidirectional reflectionless metamaterials come true by simple bending deformation based on a single arm in planar nanostructure.

Figure 3a shows a schematic of an as-designed asymmetric mirror consisting of bended metasurface, having an asymmetric reflectance from both sides to obtain the unidirectional reflectionless effect. The structure parameter of as-designed bended metasurface is also demonstrated, in which the pitch of a unit in  $x$  and  $y$  direction is  $p_x = 460$  nm and  $p_y = 900$  nm in  $x$  and  $y$  direction, respectively. Each unit cell has a bended cantilever with 150 nm ( $w$ ) in width and 600 nm ( $l$ ) in length, and the supportive frames of the unit cell have the same width of 75 nm ( $d$ ) in all directions. Before the bending process, this 2D planar pattern can be fabricated by EBL, RIE, and metal deposition. Then under moderate ion irradiation, the cantilever in the planar pattern will be bended to a controllable angle ( $\alpha$ ), as defined in Figure 3a. Based on the design of this bended metasurface, the sample of large-scale bended metasurfaces can be massively fabricated, as shown in Figure 3b.

The finite elements method (FEM) is introduced to analyze the optical properties of the bending metasurface depicted in Figure 3. Figure 4 gives the simulated results of bended metasurfaces with  $\gamma$ -polarized incidence, including transmission, reflection, and absorption spectrum, their changes with bending angle and surface current distribution. According to the transfer matrix of this metasurface,<sup>[50]</sup> the transmission spectra should totally be overlapped for backward and forward incident, and the transmission curves for 45° bending metasurface in Figure 4a prove this result primarily. In the case of reflection, a perfect unidirectional reflectionless effect is observed. For the forward incidence, a broad dip (red curve) appears at 1490 nm, indicating that the incident light is coupled by the resonance occurred in the bended metasurface. As a contrast, the broad dip for backward incidence (blue curve) is largely weakened, which clearly reflects an asymmetric resonance between backward and forward incidence appeared in this bended metasurface. The reflectance difference ( $\Delta R$ ) between forward/backward excitation is about 60% at 1490 nm, indicating a high efficiency in unidirectional reflectionless as an asymmetric mirror. In addition, the absorption of this asymmetric mirror can be calculated by  $A = 1 - T - R$ , where  $T$  and  $R$  represent the transmission and reflection of this bended metasurface, as demonstrated in Figure 4b, and the absorption by forward incidence is also much stronger than that by backward incidence. Moreover, this asymmetric resonance can be tuned with the bending angle of the cantilevers. Figure 4c depicts the simulated results of 2D reflection spectrums of as-designed bended metasurface with the increase of bending angle

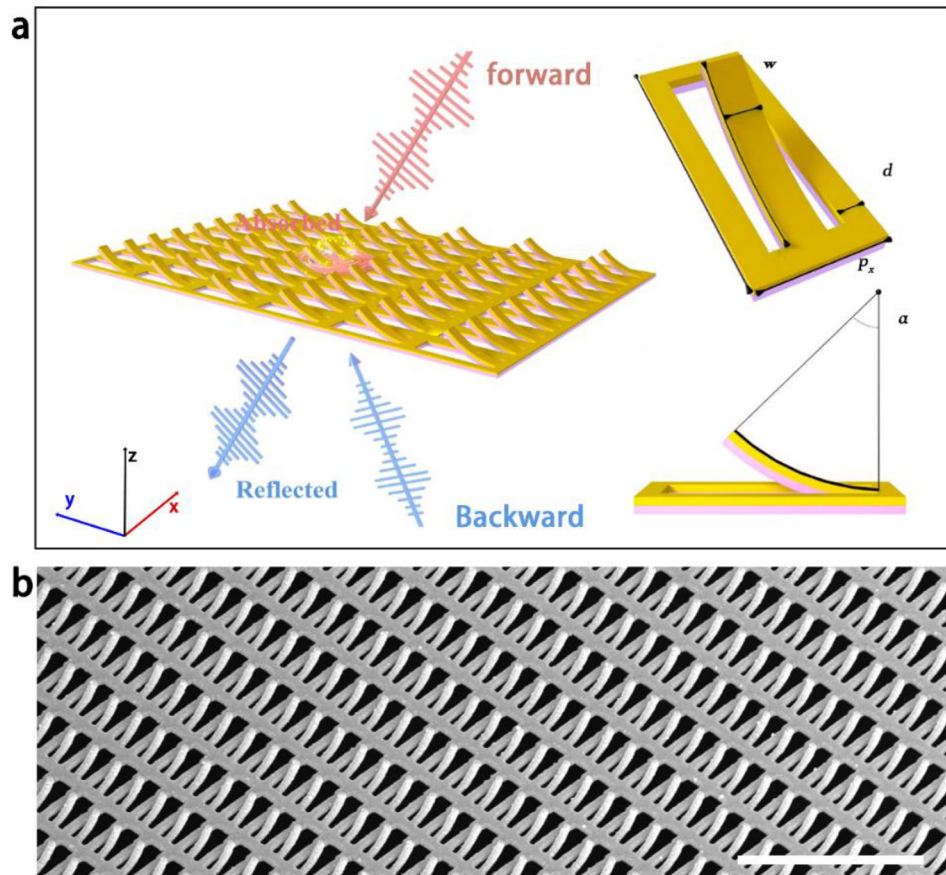


**Figure 3.** a) Schematic of as-designed bending meta-surface structure with unidirectional reflectionless effect, and the feature size and bending angle of a unit cell in the bending metasurface are defined; b) SEM image of the as-fabricated large-scale arrays of 3D bending metasurface with 45° bending angle; Scale bar: 2  $\mu\text{m}$ .

from 20° to 100°. The top and middle reflection spectrums stand for the forward and backward incidence, respectively. Clearly seeing, all the forward reflection spectrums have a reflectionless dip, but an outstanding reflection effect can be observed from backward reflection spectrums. In addition, the contrast ratio of the forward and backward reflection is calculated and shown in the bottom one of Figure 4c. A blue-shift of unidirectional reflectionless wavelength will occur with the increase of bending angle, indicating that the unidirectional reflectionless wavelength can be flexibly modulated by the bending angle. Besides, Figure S3, Supporting Information, shows the absorption spectra changes with the bending angle, where we can see a strong absorption at resonance frequency for forward incident, and a much weaker absorption is observed for backward incident. This indicates the asymmetric resonance wavelength changes with bending angle.

Moreover, we focus on discussing the mechanism behind asymmetric resonance in this bending metasurface. The surface current distribution at 1490 nm of this bended metasurface with  $\alpha = 45^\circ$  is extracted by FEM, as manifested in Figure 4d. The simulation results indicate that both the rectangular metallic supportive frame and the curly cantilevers are simultaneously excited by forward (backward)  $\gamma$ -polarized incident waves while the induced surface current is in the opposite (same) direction. The antiparallel surface current, ascribed to the phase

difference of the induced surface current in supportive frame and the curly cantilevers, means the vanishing of the electric dipole response, which results in the near-zero reflection under forward  $\gamma$ -polarized illumination.<sup>[53,54]</sup> In this case, the incident energy is cancelled through the strong near-field interaction (Figure S4, Supporting Information) and the incident energy is consumed by metal loss and radiation loss. For backward  $\gamma$ -polarized illuminations, the surface current in the rectangular metallic frame and the curly cantilevers are parallel that results in a high reflectance. This asymmetric resonance mechanism in this bended metasurface is entirely different from traditional mechanism of as-reported multilayer structures or parity-time symmetric (PT) optical systems, giving a new perspective to realize asymmetric mirror by simple bended metasurface.

To verify the simulated and analysis results above, the experimental measurement of the transmission/reflectance spectrum for bended metasurface are carried out, as shown in Figure 5. The transmission/reflectance spectrum of as-fabricated bended metasurface with a 45° bending angle (the sample is displayed Figure 3d) under the forward and backward incidence are displayed in Figure 5a. The results indicate clearly a very strong unidirectional reflectionless property induced by asymmetric resonance mechanism in the bending structure, and the experimental  $\Delta R$  is 56% with a reflectance of 62% for backward



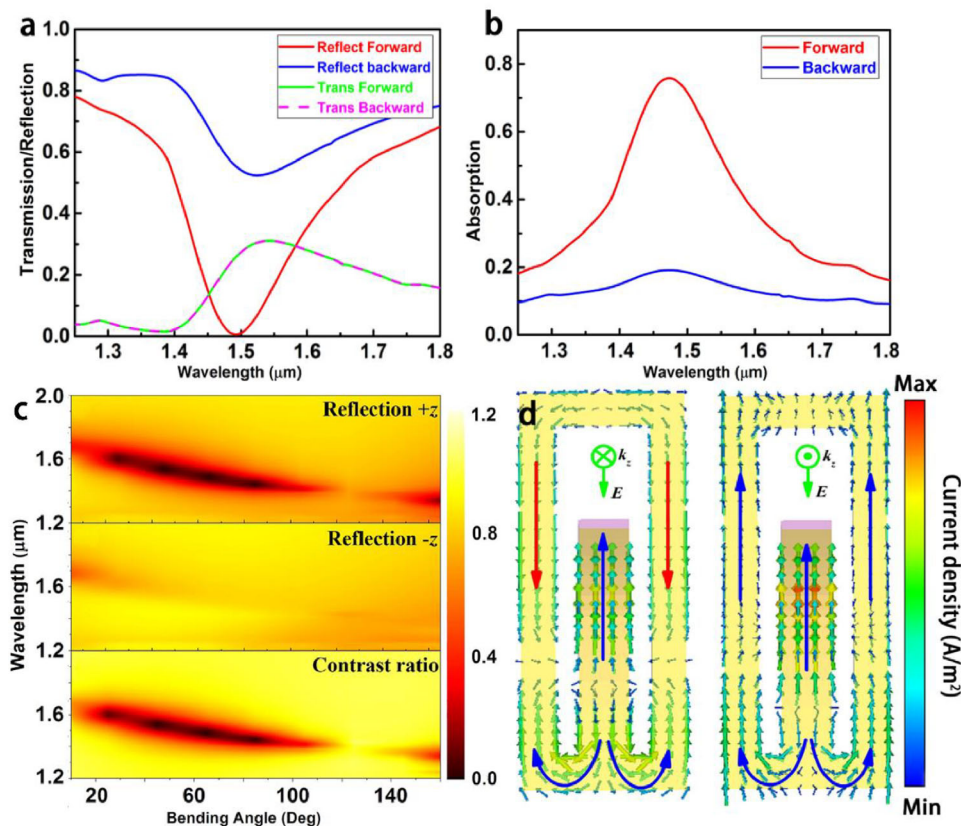


**Figure 4.** a) Simulated transmission/reflectance and b) absorption spectrum of a bended metasurface with 45° bending angle under the forward and backward incidence; c) As-simulated 2D spectrum of the bended metasurface changed with different bending angle. From top to the bottom, the reflectance spectrum of forward incidence, backward incidence, and the contrast ratio of forward/backward are ordered, respectively; d) Surface current distribution of the bended metasurface at the incidence of 1490 nm.

incidence and 6% for forward incidence, which is close to the simulated result of 60%. Besides, the absorption curves shown in Figure 5b match the simulated curves quite well. Thus, for this bended metasurface, the experimental results have a good consistency with simulated results. In addition, the bending angle of bended metasurface can be changed to tune the reflectance spectra, and a series of the samples with different bending angles ranged from 30° to 120° are fabricated and displayed in Figure 5c. Figure 5d shows a set of reflectance spectra of bended metasurface with different bending angles, and there is a remarkable blue-shift with the increasing of  $\alpha$ . When the bending angle is 30°, the resonance is at 1425 nm, and it is blue-shifted to 1375 nm when the bending angle reaches 120°, but the reflectance still maintains a low value despite the changing of bending angle. Figure 5e shows the measured  $\Delta R$  as a function of bending angle. With the bending angle ranging from 30° to 90°, the  $\Delta R$  keeps a high value of over 45%, indicating a large window to tolerate the change of bending angle and sustain efficient unidirectional reflectionless performance. Interestingly, the reflection difference increases first and then decreases with the increase of the bending angle, this is because the unidirectional reflectionless effect comes from the antiparallel distribution of the surface current which changes with the bending angle. We also have taken note of a mismatch of resonance peak position between the simulation and experiment. In addition to imperfect fabrication

and the noise from background in the measurement process, this inconsistency of peak position may be mainly attributed to the change of surface morphology induced by high-energy ions dose implantation, such as the increase of Au grains size and surface roughness, producing directly obvious enhanced scattering effect and hence influencing the optical property. Besides, the reflection spectra also become higher for both forward incident and backward incident because of the background noise.

The incident angle depended reflection property is also discussed by FEM simulation, as shown in Figure 6. We observe that when the incident angle changes from  $-20^\circ$  to  $20^\circ$  for TE and TM polarization, the modulation depth and resonance wavelength of the asymmetric resonance peak are broadly stable. This result reveals that the asymmetric resonance is not very sensitive to the incident angle, only if the polarization of the incident electromagnetic wave is along the direction of the cantilever. This is because the electric filed component of the incident light that leads to the asymmetric resonance in the  $x$ - $y$  plane keeps unchanged for these bended metasurface, and the contribution of the electric filed component along  $z$ -axis is negligible for this resonance. As a result, the resonance position depicts a stabilization in the oblique incident of light even for the incident angle up to  $20^\circ$ . A slight shift can also be observed for both TE and TM incident. For TM incident, an additional optical path difference

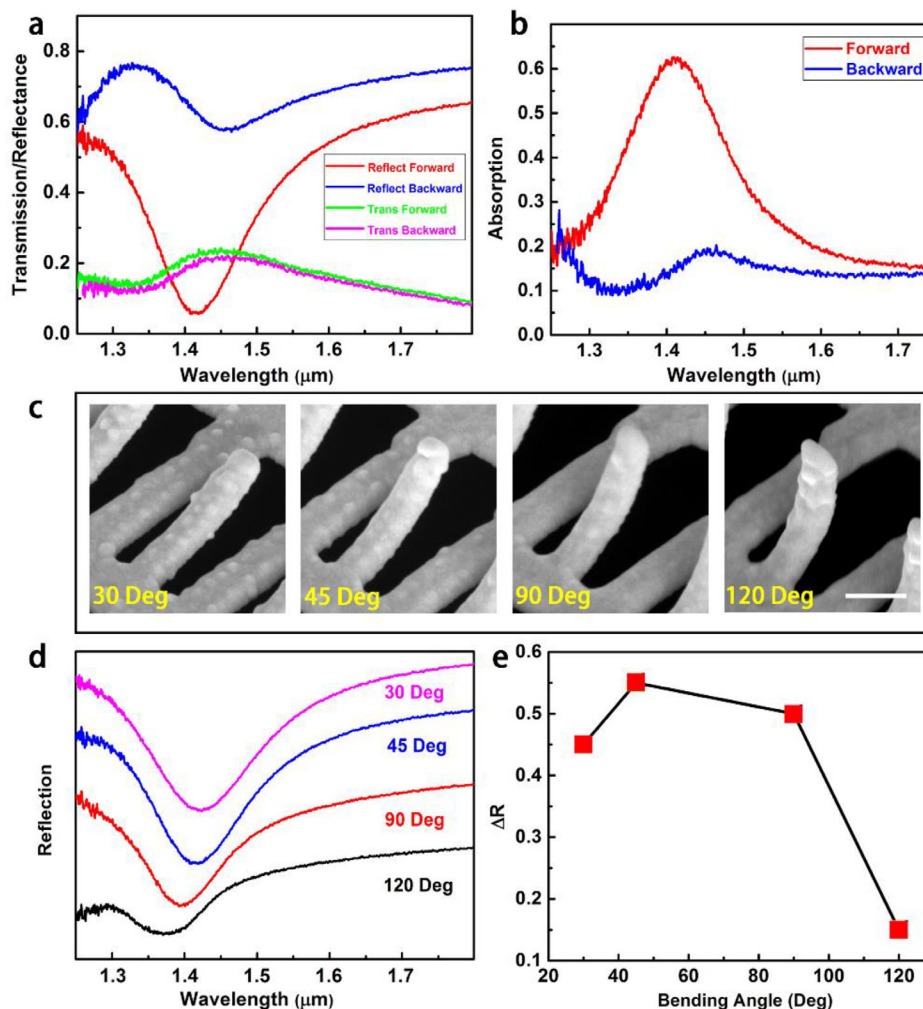


**Figure 5.** Experimental results of as-fabricated bended metasurface. a) Transmission/reflection spectrum and b) absorption spectrum of a bended metasurface with a 45° bending angles; c) Enlarged SEM images of a unit of 3D bended structures with different bending angles of 30°, 45°, 90° to 120°, respectively; Scale bar: 200 nm. d) Change of the reflected spectrum of bended metasurface with different bending angle for forward incidence with  $\gamma$ -polarization; e) Reflectance difference ( $\Delta R$ ) between the forward and backward incidence versus bending angles.

(OPD) would be introduced into the structure, this OPD will have an effect on the resonance position, the wavelength increases for a large incident angle. And for TE incident, the magnetic component of the light along  $z$ -axis could produce some new resonance whose wavelength is smaller than the unidirectional reflectionless wavelength, thus the resonance wavelength decreases with the bending angle increase.

In general, the performance of the asymmetric mirror based on bended metasurface is quite promising compared with those by traditional approaches. Previously reported asymmetric mirrors assembled by multilayer material<sup>[55]</sup> usually have a weaker  $\Delta R$  than 56% in this work. Although the unidirectional reflectionless metamaterials based on the concept of PT symmetric systems can reach a  $\Delta R$  of 60% by the simulation, the practical measurement is limited by the rigorous test conditions that need the light to be coupled to the PT metamaterials on the  $x$ - $y$  plane.<sup>[50,56]</sup> By contrast, the bended metasurface with free bending angle provides a simple strategy and new mechanism to realize a brilliant feature of 56%  $\Delta R$  that meets the need in practical application.

And more importantly, it has a robust performance regarding the incident angle of light, which can hardly be found in other kinds of asymmetric mirrors. The 3D bending structures are also suitable for the assembly of a series of optical devices operating in NIR region, such as Fano-resonance devices, plasmonic induced transparency devices, and chiral optical antennas. We believe that FIB-defined origami method for constructing bended metasurface will inspire the design of 3D substrate-free metamaterials with a host of novel properties and open up a new horizon in various fields.

### 3. Conclusion

We proposed a FIB-defined origami fabrication method with a brand new strategy to construct rapidly a large-scale 3D micro/nanostructures from desirable substrate-free 2D patterns. Benefits from this micro/nano-origami fabrication, including main bending mode together with folding mode, versatile 3D



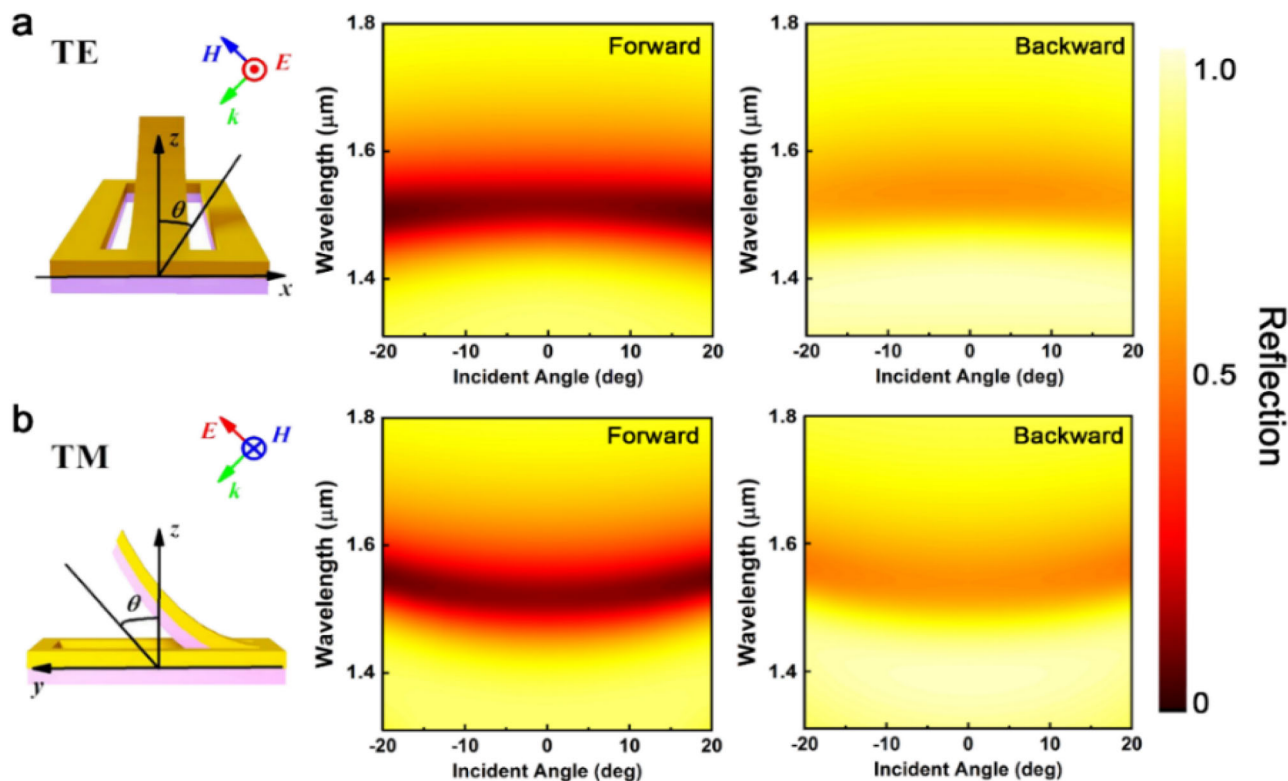


**Figure 6.** a) For TE incidence, the 2D reflection spectrum of the 45° bending metamaterials versus the incident angle, the spectrum in the left and the right indicates the reflectance of forward and the backward incidence; and b) the reflectance versus the incident angle of TM incidence.

spatial structure configurations, with a curvature radius down to 175 nm, can be designed and realized, presenting spatial structural states including cross bending and rolling, bistable, twisting, and multidimensional complex structures controlled by combining the bending with folding mode. The mechanism behind FIB-defined origami is the residual stress introduced by FIB irradiation and implantation, in which surface-layer tensile stress plays a critical part in the whole bending deformation. Importantly, FIB area-irradiation and local-irradiation can define the bending and folding deformation, respectively. Compared with the folding process, FIB-defined bending process has an extremely high efficiency in fabrication with a smaller ion dose and in very short time. The bending curvature can be continuously tuned in a rather wide range by the irradiation dose, ion energy, the thickness of the films, and even geometrical shape of 2D patterns. Based on FIB-defined bending toward an application of optical metasurface, an asymmetric mirror is designed and achieved by a 3D bending metasurface with bended cantilever structure, providing a very simple strategy to obtain a strong near-infrared unidirectional reflectionless effect with high reflection efficiency of 56% due to the asymmetric plasmonic resonance. Moreover, this FIB-defined rapid origami in micro/nanoscale could fully combine with the advantage of mature planar nanofabrication, opening up a new horizon for the practical application of diversiform stereo-metamaterials, and also build up robust platform to configure versatile 3D functional structure over wider areas in micro-nanoscale photonic, mechanical, and photoelectric device, etc.

## 4. Experimental Section

**2D Pattern Preparation:** The  $\text{SiN}_x$  windows with 20 to 100 nm film were purchased (Ilabilab Company), and the area of the windows chosen was  $100 \times 100 \mu\text{m}^2$  or  $1 \times 1 \text{mm}^2$ . First, these windows were cleaned under an oxygen plasma atmosphere by RIE for 10 s, and the pressure was maintained at 100 mTorr with 100 sccm  $\text{O}_2$  flow. Then, PMMA (495 A5) was spin-coated on the windows, and 200 nm thick PMMA film was obtained after 180 °C bake. The PMMA was patterned by electron beam lithography (EBL) and then RIE process, in which the etching duration of RIE process was 2 min under the power of 200 W, and the processing chamber maintained a 55 mTorr pressure with the gas flow of 5 sccm  $\text{O}_2$  and 50 sccm  $\text{CHF}_3$ . After that, the residual PMMA was then removed by RIE. Finally, Au with a thickness of 30–100 nm was deposited by magnetron sputtering with due thickness to obtain as-patterned metal/dielectric bilayer on the windows.

**FIB-Defined Origami:** The patterned bilayer membrane was placed into the chamber of a FIB/SEM system (Helios 600, FEI) with Ga ion source. The 2D planar patterns can be bended or folded to a 3D structure by the ion irradiation process with area-scanning or line-scanning mode. Different ion energies (8, 16, and 30 KeV) and ion beam current densities (ranged from 7 pA to 65 nA) can be optionally applied to build up various 3D structures. The in situ SEM system of the FIB/SEM system can be used to characterize the morphology of the 3D structures during the irradiation procedure. The bending angles of the architectures can be flexibly tuned from 0° to more than 180°.

**Optical Setup:** A Fourier-transform infrared spectrum (FT-IR) system (Bruke Vetex V80) was used to measure the transmission/reflectance spectrum of the metamaterials. This instrument is equipped with an NIR optical source. A sample with  $100 \times 100 \mu\text{m}^2$  area was displaced under the microscope (Bruker Hyperion) with 15× objective lens. The background signal was obtained from an 80 nm Au film for 128 times scanning, and then

the spectrum of the bended metasurfaces was obtained after 128 times scanning.

## Supporting Information

Supporting Information is available from the Wiley Online Library or from the author.

## Acknowledgements

R.P. and Z.L. contributed equally to this work. The authors acknowledge the financial support received from the National Key Research and Development Program of China (Grant No. 2016YFA0200800 and 2016YFA0200400), the National Natural Science Foundation of China (Grant No. 11674387, 11574369, 91323304, 11574368, and 11574385), and the Key Research Program of Frontier Sciences of Chinese Academy of Sciences (Grant No. QYZDJ-SSW-SLH042).

## Conflict of Interest

The authors declare no conflict of interest.

## Keywords

asymmetric mirrors, bended metasurfaces, bending deformation, focused ion beam-defined origami, residual stress

Received: May 30, 2019

Revised: September 17, 2019

Published online: November 26, 2019

- [1] J. B. Berger, H. N. Wadley, R. M. McMeeking, *Nature* **2017**, *543*, 533.
- [2] J. Ni, Z. Wang, Z. Li, Z. Lao, Y. Hu, S. Ji, B. Xu, C. Zhang, J. Li, D. Wu, J. Chu, *Adv. Funct. Mater.* **2017**, *27*, 1701939.
- [3] G. S. Park, Y. B. Kim, S. Y. Park, X. S. Li, S. Heo, M. J. Lee, M. Chang, J. H. Kwon, M. Kim, U. I. Chung, R. Dittmann, R. Waser, K. Kim, *Nat. Commun.* **2013**, *4*, 2382.
- [4] T. Buckmann, N. Stenger, M. Kadic, J. Kaschke, A. Frolich, T. Kennerknecht, C. Eberl, M. Thiel, M. Wegener, *Adv. Mater.* **2012**, *24*, 2710.
- [5] T. Ergin, N. Stenger, P. Brenner, J. B. Pendry, M. Wegener, *Science* **2010**, *328*, 337.
- [6] C. Chang, C.-F. Chiang, C.-H. Liu, C.-H. Liu, *J. Micromech. Microeng.* **2005**, *15*, 812.
- [7] M. L. Perrin, E. Burzuri, H. S. van der Zant, *Chem. Soc. Rev.* **2015**, *44*, 902.
- [8] D. Maji, D. Das, J. Wala, S. Das, *Sci. Rep.* **2016**, *5*, 17776.
- [9] B. A. Goessling, T. M. Lucas, E. V. Moiseeva, J. W. Aebbersold, C. K. Harnett, *J. Micromech. Microeng.* **2011**, *21*, 065030.
- [10] Y. Lee, A. S. A. Kamal, M. Abasaki, Y.-L. Ho, Y. Takakura, J.-J. Delaunay, *ACS Photonics* **2016**, *3*, 2405.
- [11] M. Chirumamilla, A. Toma, A. Gopalakrishnan, G. Das, R. P. Zaccaria, R. Krahn, E. Rondanina, M. Leoncini, C. Liberale, F. De Angelis, E. Di Fabrizio, *Adv. Mater.* **2014**, *26*, 2353.
- [12] K. Malachowski, M. Jamal, Q. Jin, B. Polat, C. J. Morris, D. H. Gracias, *Nano Lett.* **2014**, *14*, 4164.
- [13] J. K. Luo, R. Huang, J. H. He, Y. Q. Fu, A. J. Flewitt, S. M. Spearing, N. A. Fleck, W. I. Milne, *Sens. Actuators, A* **2006**, *132*, 346.
- [14] M. Beidaghi, Y. Gogotsi, *Energy Environ. Sci.* **2014**, *7*, 867.
- [15] R. Liu, C. Ji, J. J. Mock, J. Y. Chin, T. J. Cui, D. R. Smith, *Science* **2009**, *323*, 366.
- [16] J. Valentine, S. Zhang, T. Zentgraf, E. Ulin-Avila, D. A. Genov, G. Bartal, X. Zhang, *Nature* **2008**, *455*, 376.
- [17] Z. Liu, S. Du, A. Cui, Z. Li, Y. Fan, S. Chen, W. Li, J. Li, C. Gu, *Adv. Mater.* **2017**, *29*, 1606298.
- [18] S. H. Shams Mousavi, A. A. Eftekhari, A. H. Atabaki, A. Adibi, *ACS Photonics* **2015**, *2*, 1546.
- [19] P. Wang, O. Liang, W. Zhang, T. Schroeder, Y. H. Xie, *Adv. Mater.* **2013**, *25*, 4918.
- [20] X. Chen, N. C. Lindquist, D. J. Klemme, P. Nagpal, D. J. Norris, S. H. Oh, *Nano Lett.* **2016**, *16*, 7849.
- [21] K. V. Sreekanth, Y. Alapan, M. ElKabbash, E. Ilker, M. Hinczewski, U. A. Gurkan, A. De Luca, G. Strangi, *Nat. Mater.* **2016**, *15*, 621.
- [22] Y. Zhong, *Science* **2014**, *345*, 2.
- [23] J. L. Silverberg, A. A. Evans, L. McLeod, R. C. Hayward, T. Hull, C. D. Santangelo, I. Cohen, *Science* **2014**, *345*, 647.
- [24] Y. Liu, Z. Yan, Q. Lin, X. Guo, M. Han, K. Nan, K.-C. Hwang, Y. Huang, Y. Zhang, J. A. Rogers, *Adv. Funct. Mater.* **2016**, *26*, 2909.
- [25] S. Xu, Z. Yan, K.-I. Jang, W. Huang, H. Fu, J. Kim, Z. Wei, M. Flavin, J. McCracken, R. Wang, A. Badea, Y. Liu, D. Xiao, G. Zhou, J. Lee, H. U. Chung, H. Cheng, W. Ren, A. Banks, X. Li, U. Paik, R. G. Nuzzo, Y. Huang, Y. Zhang, J. A. Rogers, *Science* **2015**, *347*, 154.
- [26] Z. Yan, F. Zhang, F. Liu, M. Han, D. Ou, Y. Liu, Q. Lin, X. Guo, H. Fu, Z. Xie, M. Gao, Y. Huang, J. Kim, Y. Qiu, K. Nan, J. Kim, P. Gutruf, H. Luo, A. Zhao, K.-C. Hwang, Y. Huang, Y. Zhang, J. A. Rogers, *Sci. Adv.* **2016**, *2*, e1601014.
- [27] J.-N. Kuo, G.-B. Lee, W.-F. Pan, H.-H. Lee, *Jpn. J. Appl. Phys.* **2005**, *44*, 3180.
- [28] T. G. Leong, B. R. Benson, E. K. Call, D. H. Gracias, *Small* **2008**, *4*, 1605.
- [29] T. Barois, L. Tadriss, C. Quilliet, Y. Forterre, *Phys. Rev. Lett.* **2014**, *113*, 214301.
- [30] C. Py, P. Reverdy, L. Doppler, J. Bico, B. Roman, C. N. Baroud, *Phys. Rev. Lett.* **2007**, *98*, 156103.
- [31] J. L. Tan, J. Tien, D. M. Pirone, D. S. Gray, K. Bhadriraju, C. S. Chen, *Proc. Natl. Acad. Sci. USA* **2003**, *100*, 1484.
- [32] K. Kuribayashi-Shigetomi, H. Onoe, S. Takeuchi, *PLoS One* **2012**, *7*, e51085.
- [33] A. Legrain, T. G. Janson, J. W. Berenschot, L. Abelmann, N. R. Tas, *J. Appl. Phys.* **2014**, *115*, 214905.
- [34] J. H. Cho, M. D. Keung, N. Verellen, L. Lagae, V. V. Moshchalkov, P. Van Dorpe, D. H. Gracias, *Small* **2011**, *7*, 1943.
- [35] J. S. Randhawa, S. S. Gurbani, M. D. Keung, D. P. Demers, M. R. Leahy-Hoppa, D. H. Gracias, *Appl. Phys. Lett.* **2010**, *96*, 191108.
- [36] M. Huang, F. Cavallo, F. Liu, M. G. Lagally, *Nanoscale* **2011**, *3*, 96.
- [37] N. S. Rajput, Z. Tong, X. Luo, *Mater. Res. Express* **2014**, *2*, 015002.
- [38] K. Chalapat, N. Chekurov, H. Jiang, J. Li, B. Parviz, G. S. Paraoanu, *Adv. Mater.* **2013**, *25*, 91.
- [39] A. Cui, Z. Liu, J. Li, T. H. Shen, X. Xia, Z. Li, Z. Gong, H. Li, B. Wang, J. Li, H. Yang, W. Li, C. Gu, *Light: Sci. Appl.* **2015**, *4*, e308.
- [40] N. S. Rajput, A. Banerjee, H. C. Verma, *Nanotechnology* **2011**, *22*, 485302.
- [41] Z. Liu, H. Du, J. Li, L. Lu, Z.-Y. Li, N. X. Fang, *Sci. Adv.* **2018**, *4*, eaat4436.
- [42] J. K. Luo, J. H. He, Y. Q. Fu, A. J. Flewitt, S. M. Spearing, N. A. Fleck, W. I. Milne, *J. Micromech. Microeng.* **2005**, *15*, 1406.
- [43] Y. Mao, Y. Pan, W. Zhang, R. Zhu, J. Xu, W. Wu, *Nano Lett.* **2016**, *16*, 7025.
- [44] C. L. Wu, F. C. Li, C. W. Pao, D. J. Srolovitz, *Nano Lett.* **2017**, *17*, 249.

- [45] I. Utke, P. Hoffmann, J. Melngailis, *J. Vac. Sci. Technol., B: Microelectron. Nanometer Struct.–Process., Meas., Phenom.* **2008**, 26, 1197.
- [46] W. D. Nix, B. M. Clemens, *J. Mater. Res.* **1999**, 14, 3467.
- [47] O. D. Supekar, J. J. Brown, N. T. Eigenfeld, J. C. Gertsch, V. M. Bright, *Nanotechnology* **2016**, 27, 49LT02.
- [48] H. Wang, P. Li, N. Gao, K. Huang, J. Kang, L. Ji, E. Yu, *Appl. Phys. Express* **2018**, 11, 092001.
- [49] K. Huang, W. Pan, J. F. Zhu, J. C. Li, N. Gao, C. Liu, L. Ji, E. T. Yu, J. Y. Kang, *Sci. Rep.* **2015**, 5, 18331.
- [50] L. Feng, Y. L. Xu, W. S. Fegadolli, M. H. Lu, J. E. Oliveira, V. R. Almeida, Y. F. Chen, A. Scherer, *Nat. Mater.* **2013**, 12, 108.
- [51] H. Yin, R. Bai, X. Gu, C. Zhang, G. R. Gu, Y. Q. Zhang, X. R. Jin, Y. Lee, *Opt. Commun.* **2018**, 414, 172.
- [52] R. Bai, C. Zhang, X. Gu, X. R. Jin, Y. Q. Zhang, Y. Lee, *Appl. Phys. Express* **2017**, 10, 112001.
- [53] S.-Q. Li, W. Song, M. Ye, K. B. Crozier, *ACS Photonics* **2018**, 5, 2374.
- [54] X. Gu, R. Bai, C. Zhang, X. R. Jin, Y. Q. Zhang, S. Zhang, Y. P. Lee, *Opt. Express* **2017**, 25, 11778.
- [55] N. A. Kuhta, A. Chen, K. Hasegawa, M. Deutsch, V. A. Podolskiy, *Phys. Rev. B* **2011**, 84, 165130.
- [56] Y. Huang, G. Veronis, C. Min, *Opt. Express* **2015**, 23, 29882.